ESA contract
Martian Environmental Model

Ref : ESA 11369/95/NL/JG(SC)

WPII deliverable :

Technical note on GCM testing

Richard Fournier, François Forget, Matthew Collins and Frédéric Hourdin
LMD/AOPP

Approved by Olivier Talagrand January 21, 1999

Final

Abstract

This document presents tests and validation of the new parametrisations of the LMD/AOPP Martian General Circulation Model (GCM) which have been developed in the frame of the ESA contract (Ref. 11369/95/NL/JG(SC)). It also presents the validation of the GCM as a whole (comparisons to available observations) and gives elements of evaluation of the improvements with respect to previous simulations.

Contents

1 Introduction

The LMD/AOPP Martian Atmospheric General Circulation Model has been significantly improved in the frame of the ESA contract (Ref. 11369/95/NL/JG(SC)). A number of new parametrisations have been developed and the horizontal and vertical resolutions have been significantly increased (see the Detail Design Document for the GCM).

The present document describe tests and validations of the parametrisations which have been either improved or developed specifically in the frame of the ESA contract (Ref. 11369/95/NL/JG(SC)): radiative transfer, planetary boundary layer, effect of mountains on the large scale flow, low polar emissivities.

For the various parametrizations, 1) we present off-line tests, 2) 1-Dimensional tests in which the physical parametrisations are run on a vertical atmospheric column without dynamics or with simplified dynamics and 3) results of full 3D simulations performed with all the updated parametrisations.

The results are compared to the relevant observations, i. e. atmospheric temperatures retrieved from the Mariner 9 IRIS observations, brightness temperatures observed by the Viking IRTM instrument and Viking surface meteorological observations.

All comparisons are fully satisfactory and results show a significant improvement with respect to older simulations. Note in particular:

1. the improvement of the mean zonal thermal structure due to both the finer vertical grid[1] and to the use of a sophisticated scheme for representation of gravity waves and mountain drag,
2. the improvement of the representation of the thermal emission in the polar region due to the introduction of a specific scheme,
3. and moreover, the impressive ability of the new Planetary Boundary Layer Scheme to represent both the wind and the amplitude of the rapid turbulent fluctuations near the surface.

Note also that the ability of the model to run over long period has been tested by runing a one-year simulation with the spectral version at Oxford University.

2 New turbulent diffusion scheme validation

2.1 Introduction

The Turbulent Diffusion scheme is described in the Detail Design Document of the GCM. Its aim is the estimation of the following quantities :

q : wind standard deviation

K_M : wind turbulent diffusion coefficient

K_H : thermal turbulent diffusion coefficient

q is a GCM output that quantifies turbulent activity in the low atmosphere : this information is needed for simulation of realistic entry profiles as well as for description of surface conditions. K_M and K_H are inputs for the Planetary Boundary Layer scheme (see the Detail Design Document of the GCM).

2.2 Validation procedure

The Turbulent Diffusion scheme is validated against solutions of a more sophisticated model, adapted from the Mellor and Yamada (1974) 2.5 closure model (see the Detail Design Document of the GCM and Helfand and Labraga, 1988). The validation is performed on one-dimensional configurations (atmospheric columns with prescribed geostrophic winds, see Sec. 2.3). Profiles of temperature, wind and wind standard deviation are compared at various latitudes in order to check that diurnal cycles are accurately represented. The same features are also analysed on three-dimensional configurations (complete GCM simulations) and surface wind diurnal cycles are compared with observations at the Viking landers sites (see Sec. 2.3).

2.3 One-dimensional validations

A vertical atmospheric column is considered. Its height is 80 km and wind intensity and direction are imposed at the upper boundary. The evolution of other quantities is simulated with the GCM "physical" package associated with a simplified dynamic scheme that solves the following equations :

$$\frac{du}{dt} = fv - fV_g + \left(\frac{\partial u}{\partial t}\right)_{phys} \tag{1}$$

[1] One significant improvement of the model comes from the increased spatial resolution. The impact of the change of horizontal resolution is rather difficult to evaluate because of the small number of relevant observations. On the other hand, the change of vertical resolution has proven to have a very significant impact on the large scale dynamics, allowing for the explicit representation in the model of the warming of the upper polar atmosphere in the period of dust storms.

$$\frac{dv}{dt} = -fu + fU_g + \left(\frac{\partial v}{\partial t}\right)_{phys} \quad (2)$$

where u and v are the components of the horizontal wind, U_g and V_g are the components of the geostrophic wind (prescribed values), f is the Coriolis parameter and $\left(\frac{\partial u}{\partial t}\right)_{phys}$ and $\left(\frac{\partial v}{\partial t}\right)_{phys}$ are the wind component tendencies due to all "physical" phenomena (including turbulent diffusion in the planetary boundary layer). This one dimensional atmosphere model is used for detailed testing of physical parametrisation schemes : computation requirements are considerably lower than for the complete GCM and sophisticated models can be implemented for the production of reference solutions to which parametrisation outputs can be compared.

As far as turbulent diffusion is concerned, profiles of temperature, wind and wind fluctuations obtained with the proposed turbulent diffusion scheme (Detail Design Document of the GCM) could be compared with those obtained with the Mellor and Yamada 2.5 turbulent diffusion model (Mellor and Yamada, 1982), that can be considered as a good reference model for stable stratified configurations. This model, that could not be implemented in the full GCM (because of computation requirements), could easily be implemented in the one-dimensional column model under the assumption that vertical diffusion of turbulent kinetic energy is negligible compared to local sources and sinks. Simulation results are displayed in Fig. 1 to 6 for the latitudes the two Viking landing sites. Fig. 1 and Fig. 4 display the wind velocity for one-day cycle. A low level nocturnal jet develops after night fall with winds increasing above the geostrophic wind in the 100-2000 m altitude range. The physical explanation for this phenomenon is that turbulence intensity decreases strongly at night time when the planetary boundary layer is very stable : atmospheric layers that were submitted to turbulent diffusion forces find themselves submitted to the only pressure and Coriolis forces and enter a non frictional oscillation process. The oscillation frequency is latitudinal dependent : at VL1 sunrise occurs approximately at maximum wind value whereas, at VL2, the night duration corresponds approximately to the half of an oscillation period. Fig. 2 and Fig. 5 display wind standard deviations that are in accordance with these scenari : turbulent fluctuations are strong at day time and decrease rapidly at night fall ; there night variations are directly related to the nocturnal jet oscillation (maximum fluctuations at maximum wind values). Vertical profiles (including the potential temperature profiles) are given in Fig. 3 and Fig. 6.

The reference solutions displayed in these figures were obtained with a 3 mn time step and a vertical discretisation in 40 layers. The solutions of the proposed scheme were obtained with time and vertical discretisations typical of GCM runs : 30 mn time step and 25 layers. This comparison exercise ensures that the turbulent diffusion scheme allows he representation of all phenomena in both qualitative and quantitative ways very similar to a second-order closure model. Also to be mentioned are small computational expenses and strong numerical robustness.

2.4 Three-dimensional validations

Various GCM simulations were made at different seasons to check the numerical behavior of the turbulent diffusion scheme. Daily cycles of the wind standard deviation have been looked at in order to check that orders of magnitude and vertical distributions are comparable to those observed in the one-dimensional runs. Temporal variations are more difficult to analysis. Nocturnal jets are observed but local wind variations are strongly affected by geostrophic wind variations that are not negligible for time intervals of a few hours. In Fig. 7 temperature, wind and wind standard deviation in the first atmospheric layer are plotted for two typical GCM

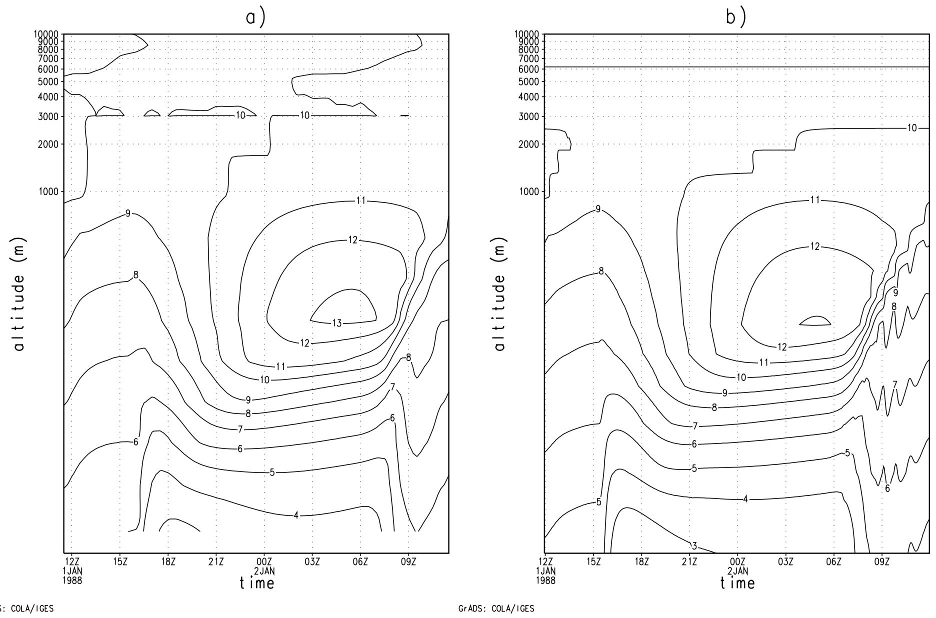

Figure 1: Horizontal wind (m/s) in the low atmosphere (one diurnal cycle from 12h to 12h) : a) proposed parametrisation ; b) Mellor and Yamada 2.5 model. Geostrophic wind : 10 m/s. Total optical thickness : $\tau_{0.67\mu m} = 1$. Season : late northern spring ($L_s = 60$). Latitude : $+22^o$.

simulations. The numerical results can be compared to the VL2 observations at a similar season (Fig. 8). For the observations, the wind standard deviation is computed on one-hour periods from the high frequency meteorological measurements recorded each 30 seconds. The structures are comparable as well as orders of magnitude. Better comparisons would require a finer horizontal discretisation.

3 New radiation scheme validation

3.1 Introduction

Several significant changes have been made to the solar and infrared radiative transfer schemes. These changes all concern the representation of dust radiative properties. The solar spectrum is now discretised in two intervals with noticeably distinct scattering properties (see Detail Design Document of the GCM). the infrared spectral discretisation has also been improved : on spectral interval for the $9\mu m$ band, two intervals for the CO2 $15\mu m$ band and one interval for large wavelengths outside the CO2 band. Apart from these spectral data changes, both the solar scheme and the CO2 infrared scheme are unchanged but the two infrared intervals outside the CO2 band are now modeled with a radiative transfer scheme that accounts for scattering by dust particles (see Detail Design Document of the GCMand Toon et al., 1989).

3.2 Validation procedure

A wide range of tests have been performed all along the procedure for determination of infrared and solar spectral data (see Detail Design Document of the GCM) : monochromatic computations were compared to IRIS measurements and average

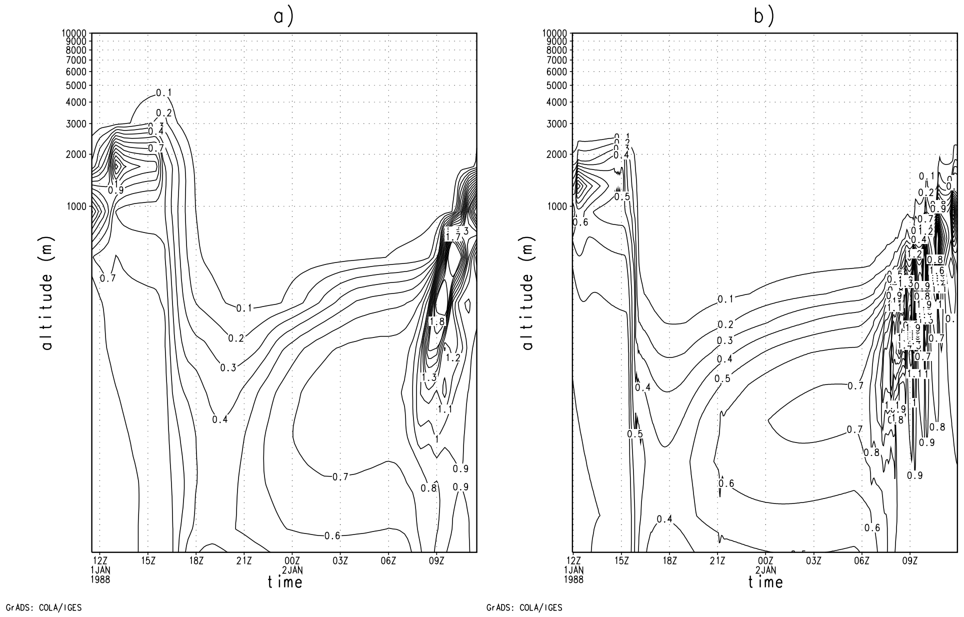

Figure 2: Wind standard deviation (m/s) in the low atmosphere (one diurnal cycle from 12h to 12h) : a) proposed parametrisation ; b) Mellor and Yamada 2.5 model. Geostrophic wind : 10 m/s. Total optical thickness : $\tau_{0.67\mu m} = 1$. Season : late northern spring ($L_s = 60$). Latitude : $+22^o$.

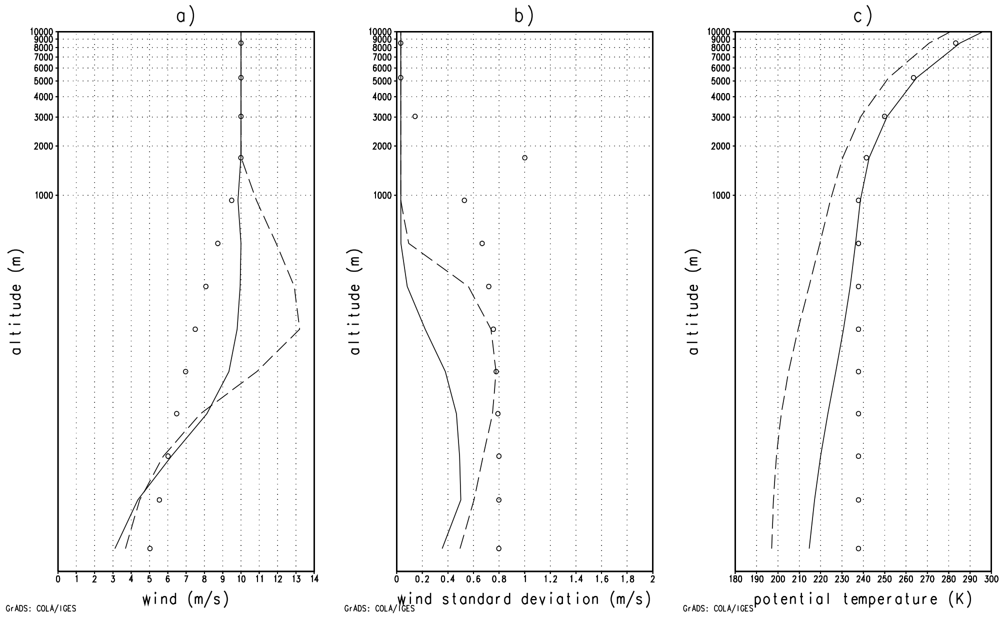

Figure 3: Vertical profiles as produced by the proposed parametrisation : a) horizontal wind (m/s) ; b) wind standard deviation (m/s) ; c) potential temperature (K). Geostrophic wind : 10 m/s. Total optical thickness : $\tau_{0.67\mu m} = 1$. Season : late northern spring ($L_s = 60$). Latitude : $+22^o$. Solid lines : local time = 21h. Broken lines : local time = 6h. Dots : local time = 15h.

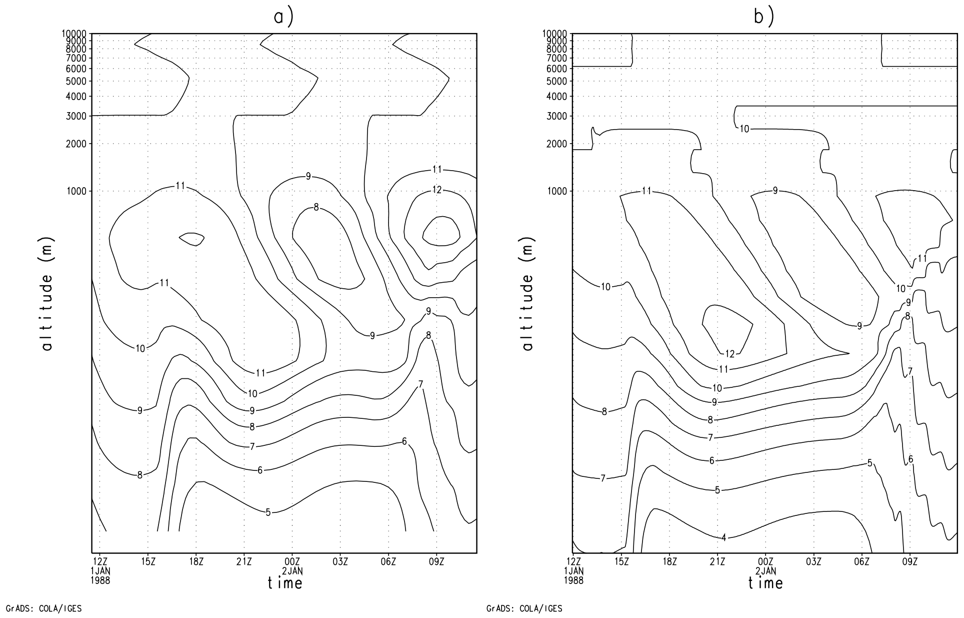

Figure 4: Horizontal wind (m/s) in the low atmosphere (one diurnal cycle from 12h to 12h) : a) proposed parametrisation ; b) Mellor and Yamada 2.5 model. Geostrophic wind : 10 m/s. Total optical thickness : $\tau_{0.67\mu m} = 1$. Season : late northern spring ($L_s = 60$). Latitude : $+48^o$.

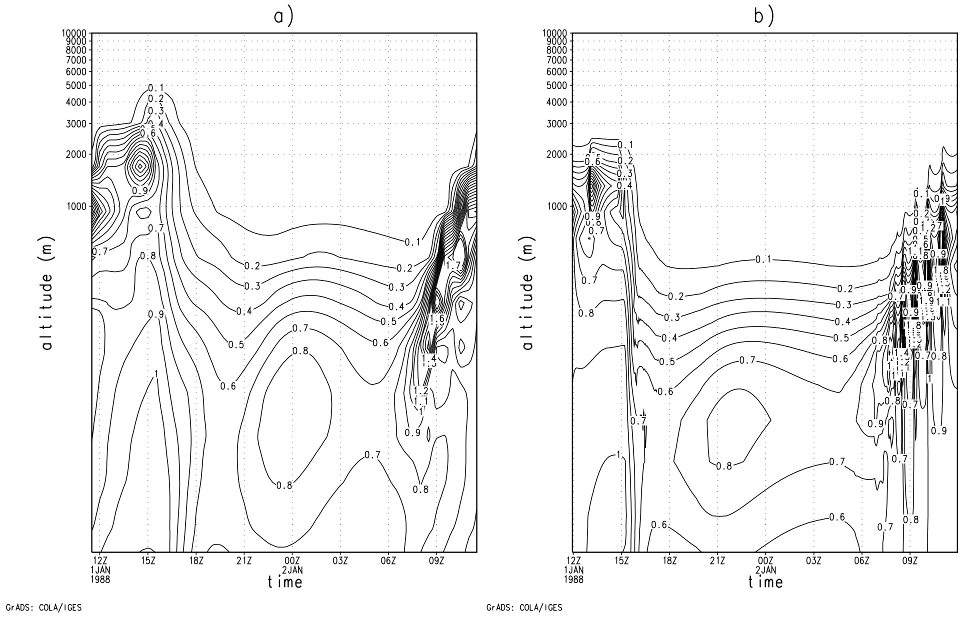

Figure 5: Wind standard deviation (m/s) in the low atmosphere (one diurnal cycle from 12h to 12h) : a) proposed parametrisation ; b) Mellor and Yamada 2.5 model. Geostrophic wind : 10 m/s. Total optical thickness : $\tau_{0.67\mu m} = 1$. Season : late northern spring ($L_s = 60$). Latitude : $+48^o$.

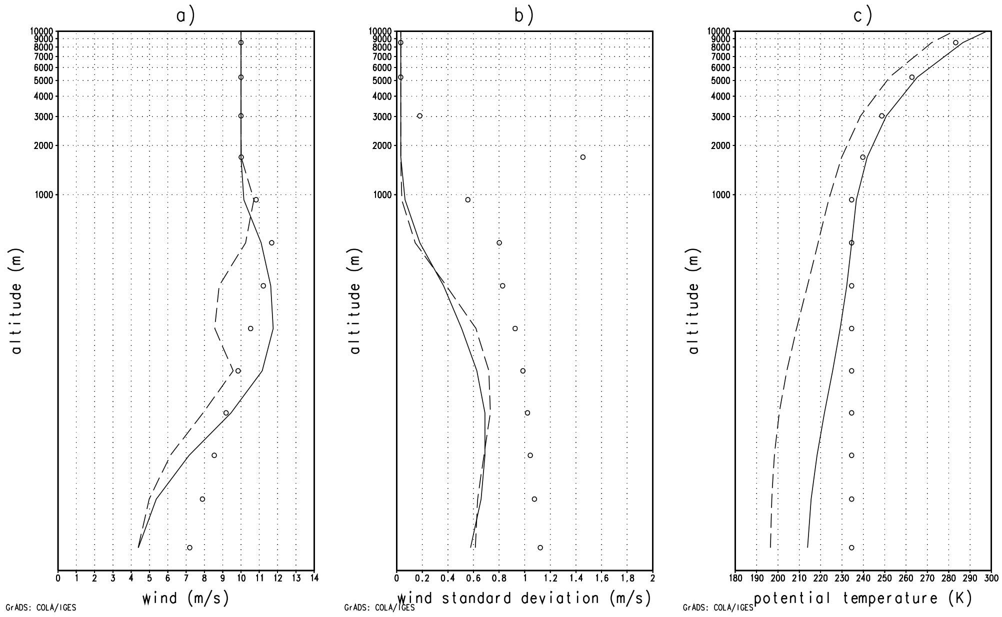

Figure 6: Vertical profiles as produced by the proposed parametrisation : a) horizontal wind (m/s) ; b) wind standard deviation (m/s) ; c) potential temperature (K). Geostrophic wind : 10 m/s. Total optical thickness : $\tau_{0.67\mu m} = 1$. Season : late northern spring ($L_s = 60$). Latitude : $+48^o$. Solid lines : local time = 21h. Broken lines : local time = 6h. Dots : local time = 15h.

spectral data were chosen such that wide band spectral discretisation introduces less than 10% errors. The radiative transfer scheme has therefore undergone severe coherence testings as well as detailed confrontations to available measurement data. Further tests were however required to make sure that the complex interfacing with the GCM structure was properly designed. A convenient way of testing this interface consisted in degrading the new scheme in order to emulate the old scheme behavior and obtain a satisfactory convergence (Sec. 3.3). This convergence exercise was performed both in the one dimensional and full three dimensional GCM versions.

3.3 Convergence with the old radiation scheme

In order to emulate the radiative transfer scheme used in the former GCM version, the radiative transfer scheme is degraded step by step the following way :

i) The two solar spectral intervals are attributed the same spectral data as those of the unique spectral interval of the old solar scheme : optical thickness - $\tau_{Sol} = \tau_{0.67\mu m}$; single scattering albedo - $\Omega_{Sol} = 0.86$; asymmetry factor - $g_{Sol} = 0.79$.

ii) The four infrared spectral intervals are attributed the same dust optical thickness : $\tau_{IR} = 0.2\tau_{Sol}$.

iii) The two infrared spectral intervals outside the CO2 band are attributed a zero single scattering albedo. This way the scattering scheme emulates a non scattering grey infrared radiative transfer scheme.

With this set of changes, the new radiative transfer scheme should produce outputs very similar to the outpus of the old scheme. Such a comparison is proposed in Fig. 9 for Seifs entry temperature profile. Solar fluxes must be identical as the solar scheme was not changed. Infrared fluxes are very similar and the remaining difference can be attributed to the way angular integrations are performed in

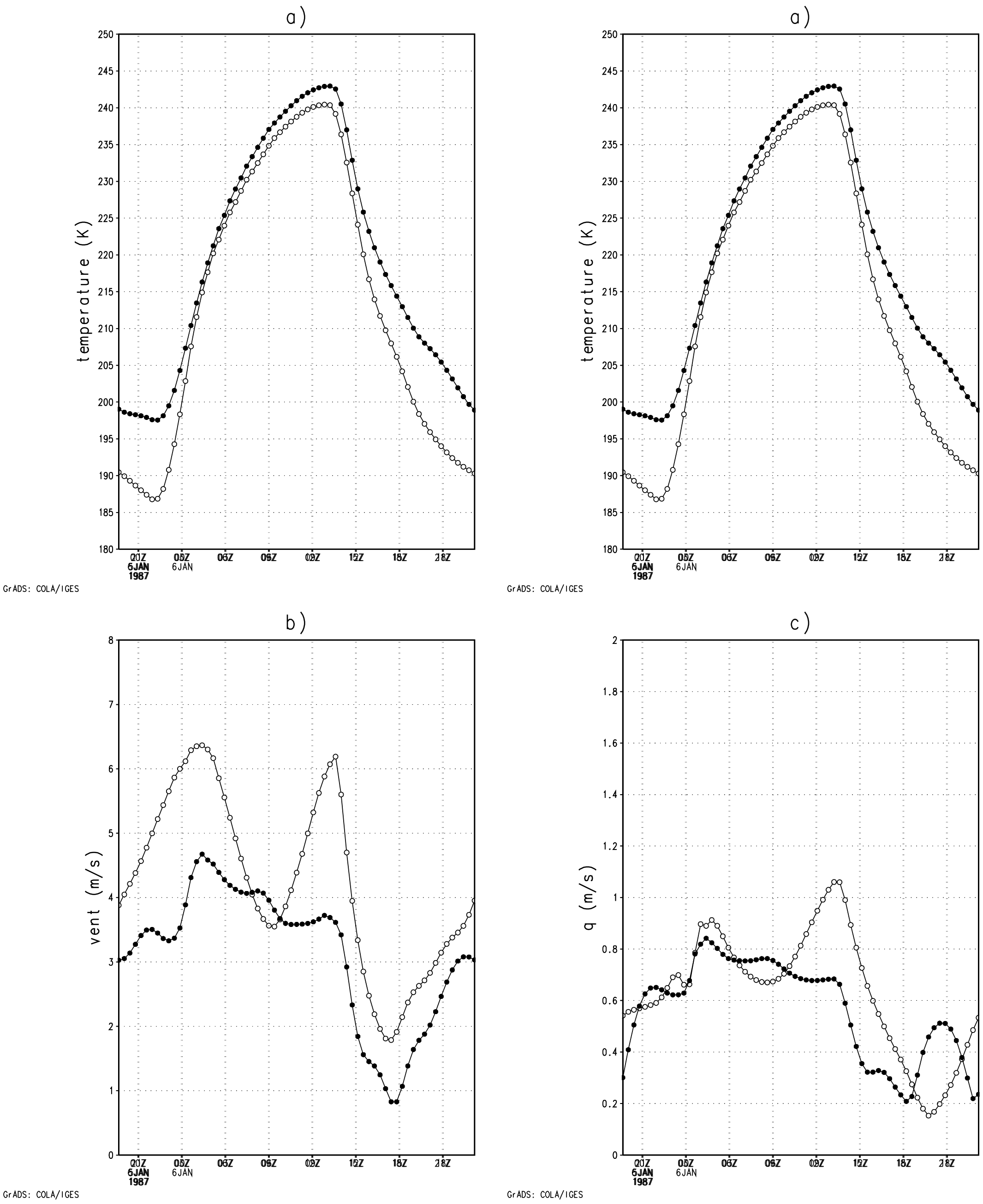

Figure 7: Typical near surface diurnal evolution of temperature (a), wind (b) and wind standard deviation (c) at latitude 48^o as simulated by the GCM with the new turbulent diffusion scheme.

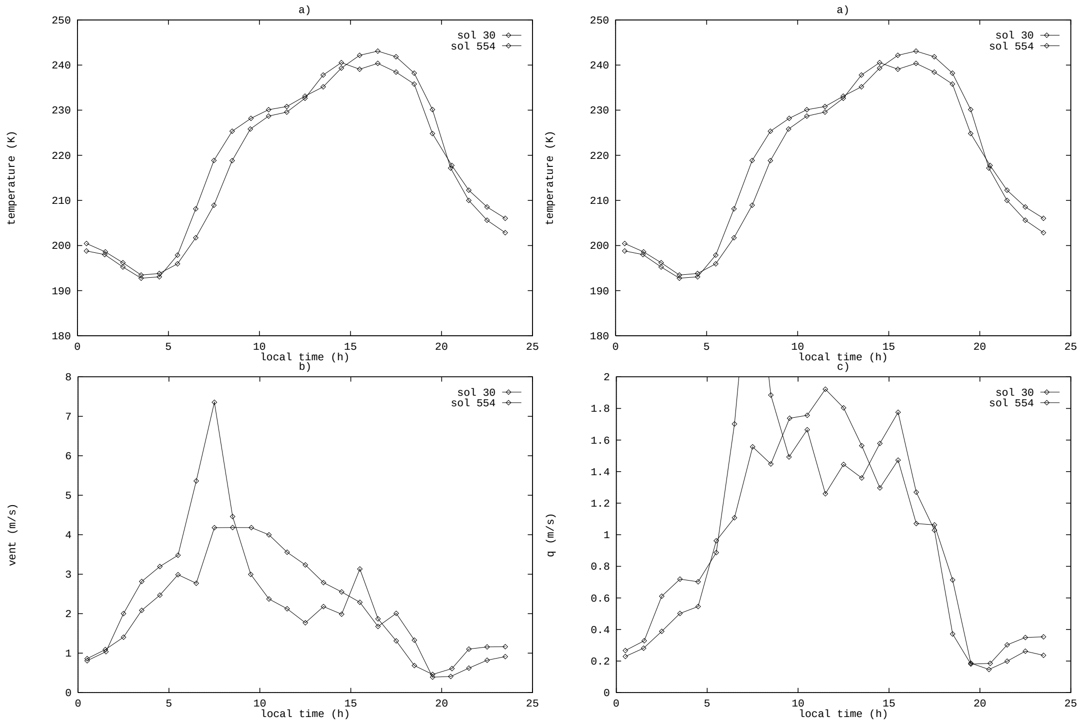

Figure 8: Typical near surface diurnal evolution of temperature (a), wind (b) and wind standard deviation (c) at latitude 48^o as observed at VL2 site

both schemes : the new scheme assumes isotropy on each hemisphere whereas the old scheme assumes that average radiation occurs at a azimuth angle θ such that $(\cos\theta)^{-1} = 1.66$. this difference is far beneath the expected precision and the convergence exercise can be considered successful. The convergence is also checked on equilibrium profiles of the one dimensional column model used for validation of the turbulent diffusion scheme. The one dimensional model is run with Seifs temperature profile for initial conditions and a 10 m/s geostrophic wind ; the diurnal cycle is not represented and solar forcing is fixed to its average value. Fig. 10-a shows the evolution of the surface temperature until equilibrium and Fig. 10-b shows the atmospheric temperature profile at one dimensional equilibrium. Here again differences between the old scheme and the degraded new scheme are beneath expectable accuracies.

Following figures show the corresponding results when the new scheme is set back to its full version. Upgrades are made step by step to illustrate the effects of each new feature. From the degraded version the solar spectral data are first set to there new values (Fig. 11 and Fig. 12). Then infrared optical thickness is set, in each band, to its new value multiplied by one minus the single scattering albedo ($\tau = \tau_i(1 - \Omega_i$, $\Omega = 0$, see Detail Design Document of the GCM) : this way we identify the effects of new spectral data with a non scattering scheme (Fig. 13 and Fig. 14). Finally the model is set to its final version by activation of the scattering algorithm ($\tau = \tau_i$, $\Omega = \Omega_i$, $g = g_i$) in the two infrared intervals outside the CO2 band (Fig. 15 and Fig. 16). Conclusions are : i) new solar spectral data represent stronger scattering by dust particles (less heating of the low atmosphere) ; ii) new infrared spectral data represent smaller infrared optical thicknesses (less cooling to space) ; iii) infrared scattering is essentially important for the prediction of surface temperatures that take higher equilibrium values.

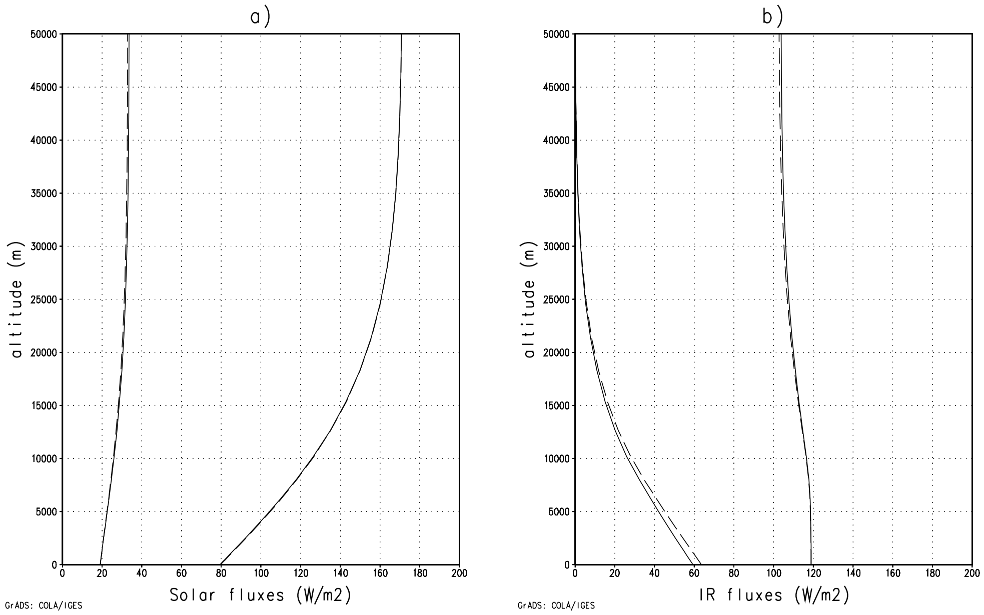

Figure 9: Upward and downward fluxes : a) solar radiation ; b) infrared radiation. Temperature profile : Seifs entry profile. Total optical thickness : $\tau_{0.67\mu m} = 2$. Season : late northern spring ($L_s = 60$). Latitude : $+22^o$. Solid lines : results of the old radiation scheme. Broken lines : results of the degraded new radiation scheme (convergence).

The same tests were performed in the full three dimensional GCM with identical conclusions.

4 Representation of Sub-Grid Scale Orography

4.1 Validation of the Sub-grid Scale Orographic Scheme

Validation of the sub-grid scale orographic scheme is hampered by the lack of observations of the Martian atmosphere. Ideally one would require observations of the pressure drag across a mountain to validate the low-level drag component (?, e.g.,) and a 4D climatology of upper level wind and temperature observations to validate the gravity wave drag component (Palmer et al., 1986, e.g.,).

Both schemes are at least based on physical arguments so we may make order of magnitude estimates of the 'tunable' parameters. However the model climatology may be sensitive even to small changes in these parameters and this must be investigated. The legitimately tunable parameters in the sub-grid scale orographic scheme are, C_d, the low level drag coefficient, H_{NC}, the critical non-dimensional mountain height, G, which multiplies the expression for the gravity wave surface stress, and Ri_c, the critical Richardson number. Theoretical considerations would lead us to choose values of 1.0, 1.0, 1.0 and 0.25 respectively for these parameters.

Validation Strategy: Mariner 9 IRIS Temperatures

The direct impact of the sub-grid scale orographic scheme, and in particular the gravity wave drag component of the scheme, is on the wind field of the model. The most noticeable effect is likely to be a deceleration of the upper level zonal winds as is seen in the terrestrial mesosphere (Andrews et al., 1987, e.g.,) page 305). There is no climatology of upper level wind observations of Mars, however there are various climatologies of temperature from remote sounding instruments and we can exploit

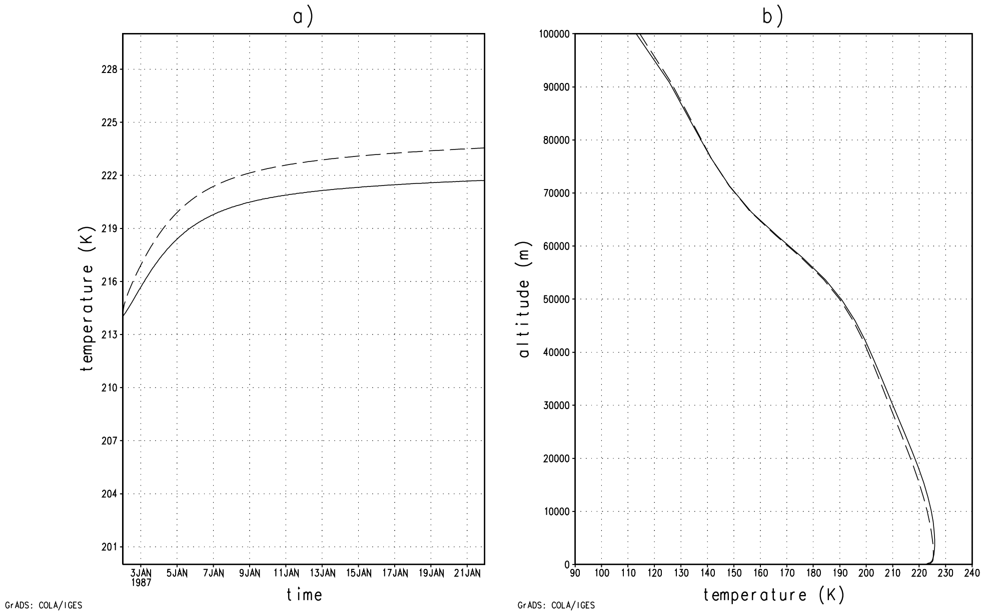

Figure 10: Solution at equilibrium of the one dimensional column model with a 10 m/s geostrophic wind : a) temporal evolution of the surface temperature for a 10 days simulation with Seifs entry profile as start profile ; b) equilibrium temperature profile. Total optical thickness : $\tau_{0.67\mu m} = 2$. Season : late northern spring (L_s = 60). Latitude : $+22^o$. Solid lines : results of the old radiation scheme. Broken lines : results of the degraded new radiation scheme (convergence).

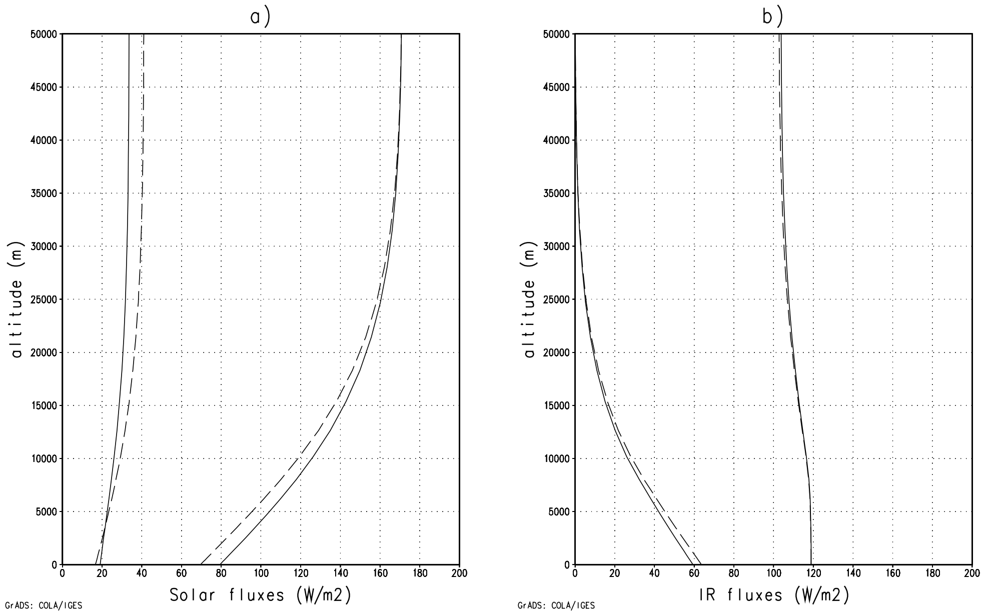

Figure 11: Upward and downward fluxes : a) solar radiation ; b) infrared radiation. Temperature profile : Seifs entry profile. Total optical thickness : $\tau_{0.67\mu m} = 2$. Season : late northern spring ($L_s = 60$). Latitude : $+22^o$. Solid lines : results of the old radiation scheme. Broken lines : results of the new radiation scheme without scattering and without the new infrared spectral data.

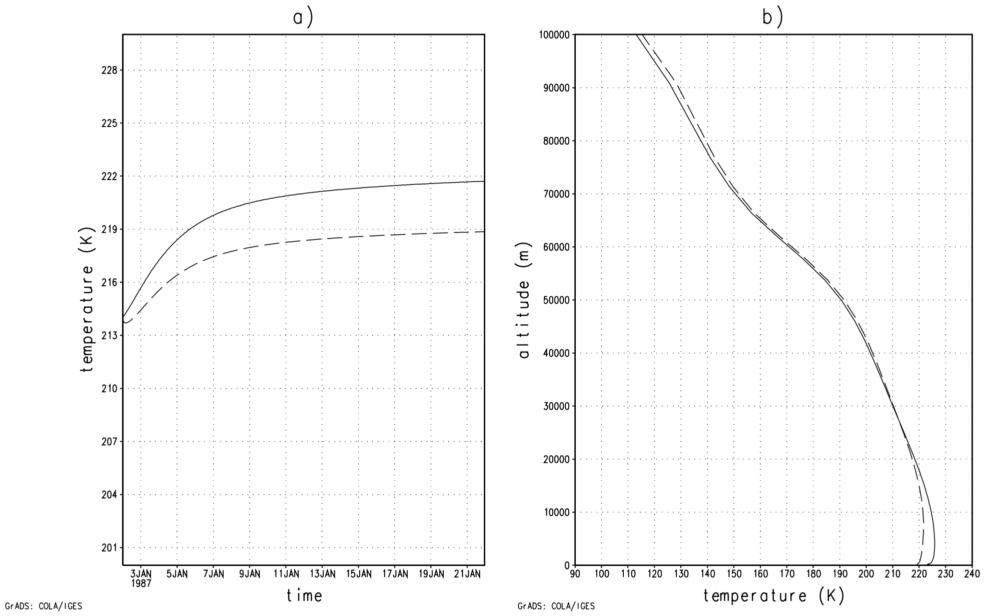

Figure 12: Solution at equilibrium of the one dimensional column model with a 10 m/s geostrophic wind : a) temporal evolution of the surface temperature for a 10 days simulation with Seifs entry profile as start profile ; b) equilibrium temperature profile. Total optical thickness : $\tau_{0.67\mu m} = 2$. Season : late northern spring ($L_s = 60$). Latitude : $+22^o$. Solid lines : results of the old radiation scheme. Broken lines : results of the new radiation scheme without scattering and without the new infrared spectral data.

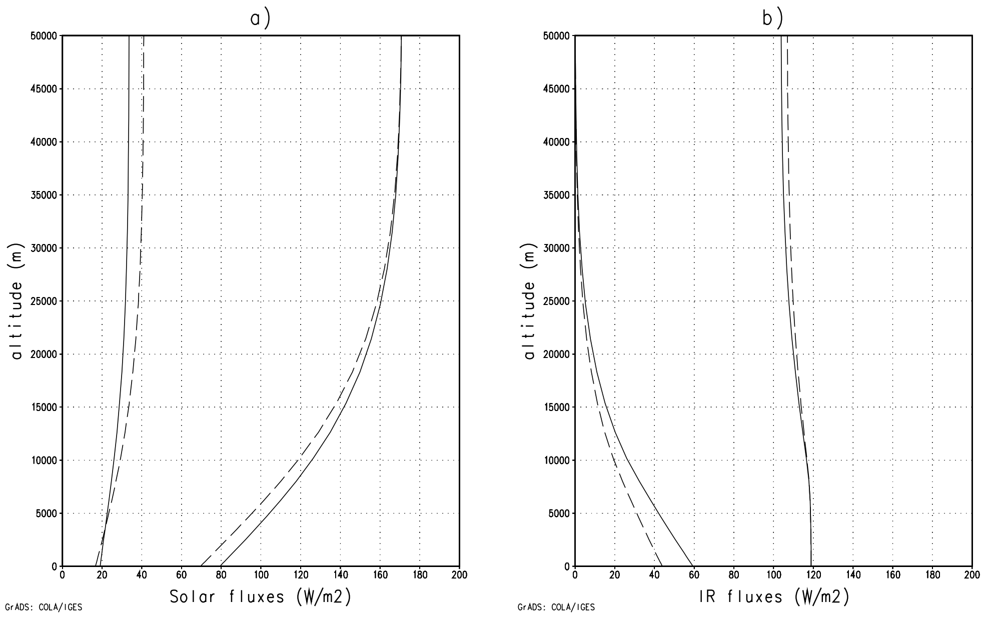

Figure 13: Upward and downward fluxes : a) solar radiation ; b) infrared radiation. Temperature profile : Seifs entry profile. Total optical thickness : $\tau_{0.67\mu m} = 2$. Season : late northern spring ($L_s = 60$). Latitude : $+22^o$. Solid lines : results of the old radiation scheme. Broken lines : results of the new radiation scheme without scattering.

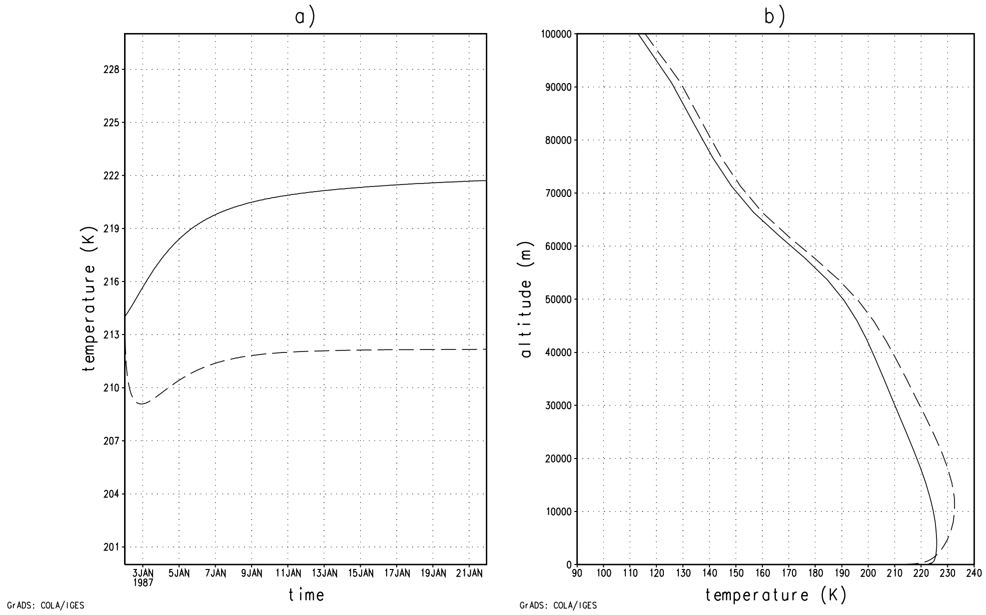

Figure 14: Solution at equilibrium of the one dimensional column model with a 10 m/s geostrophic wind : a) temporal evolution of the surface temperature for a 10 days simulation with Seifs entry profile as start profile ; b) equilibrium temperature profile. Total optical thickness : $\tau_{0.67\mu m} = 2$. Season : late northern spring ($L_s = 60$). Latitude : $+22^o$. Solid lines : results of the old radiation scheme. Broken lines : results of the new radiation scheme without scattering.

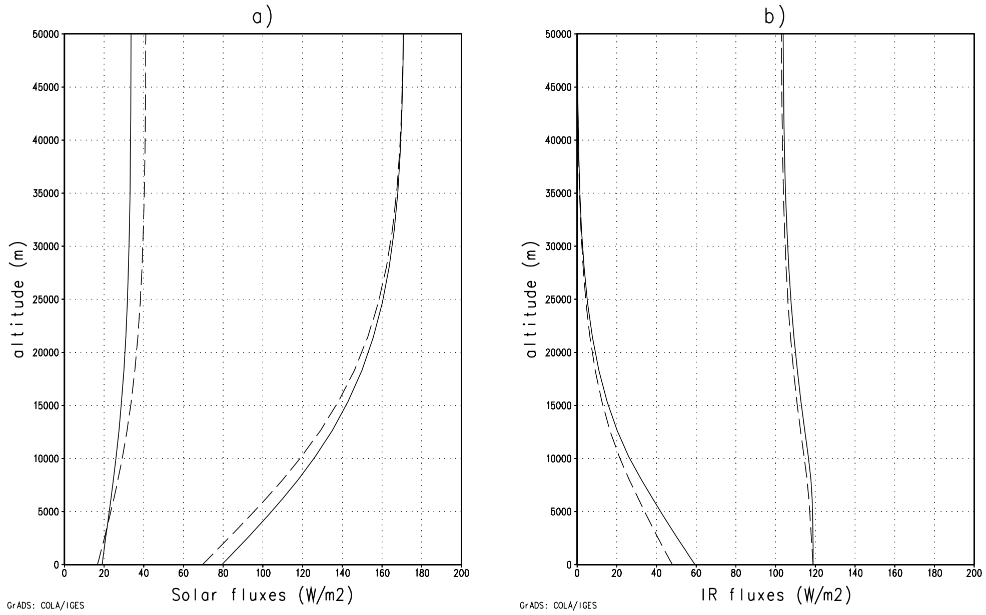

Figure 15: Upward and downward fluxes : a) solar radiation ; b) infrared radiation. Temperature profile : Seifs entry profile. Total optical thickness : $\tau_{0.67\mu m} = 2$. Season : late northern spring ($L_s = 60$). Latitude : $+22^o$. Solid lines : results of the old radiation scheme. Broken lines : results of the new radiation scheme.

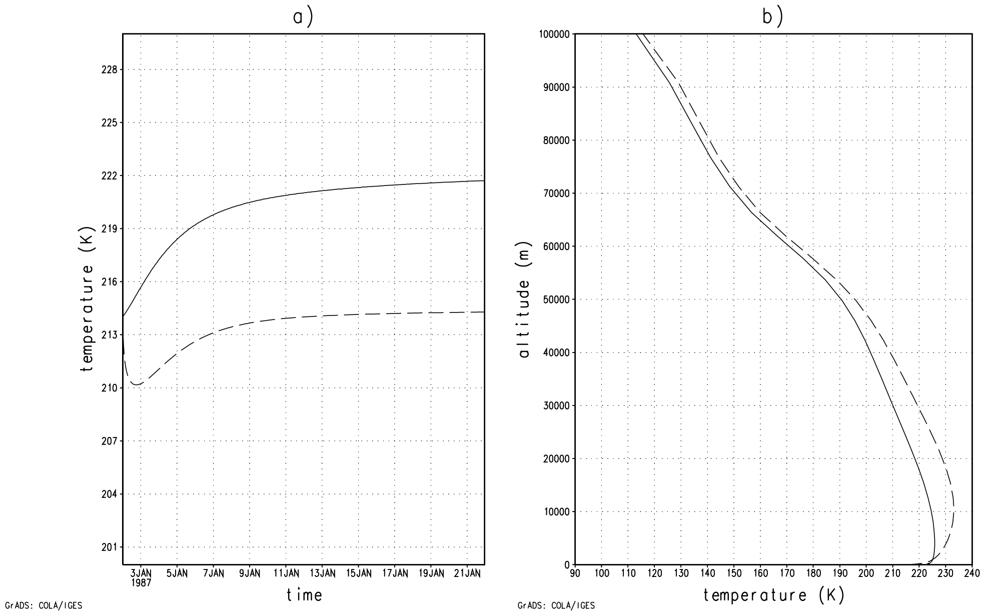

Figure 16: Solution at equilibrium of the one dimensional column model with a 10 m/s geostrophic wind : a) temporal evolution of the surface temperature for a 10 days simulation with Seifs entry profile as start profile ; b) equilibrium temperature profile. Total optical thickness : $\tau_{0.67\mu m} = 2$. Season : late northern spring ($L_s = 60$). Latitude : $+22^o$. Solid lines : results of the old radiation scheme. Broken lines : results of the new radiation scheme.

these in the validation process by noting that the gravity wave drag will have an *indirect* effect on the temperatures via dynamical balance.

We consider an atmosphere in thermal wind balance with a radiatively determined temperature state T which is warm near the equator and cold at the pole. Thermal wind balance gives us a relationship between the zonal wind shear $\frac{\partial u}{\partial z}$ and the latitudinal temperature gradient $\frac{\partial T}{\partial \phi}$ (e.g., Andrews et al., 1987, pg. 226)

$$f\frac{\partial u}{\partial z} \;=\; -\frac{R}{aH}\frac{\partial T}{\partial \phi} \tag{3}$$

where f is the coriolis parameter, R is the gas constant, a is the radius of Mars and H is the pressure scale height. If we assume that $u = 0$ at the surface and that T is independent of height, then the zonal wind shear is positive and constant with height.

Now consider what happens when a stationary gravity wave propagates vertically and breaks at upper levels. The gravity wave drag induces a negative acceleration on the zonal wind at upper levels and the shear is reduced, possibly reversed if the drag is large enough. Although thermal wind balance (equation 3) does not strictly hold in the presence of gravity wave drag, it is instructive to consider what would happen if it did. With the reduced shear at upper levels the latitudinal temperature gradient, $\frac{\partial T}{\partial \phi}$ is reduced, and again possibly reversed if the drag is large enough. Hence the gravity wave drag has a measurable effect on temperature and we can use this to validate the sub-grid scale orographic scheme.

We have chosen to use the temperature fields retrieved from the Mariner 9 IRIS instrument by Santee and Crisp (1993). The temperatures are near global in cov-

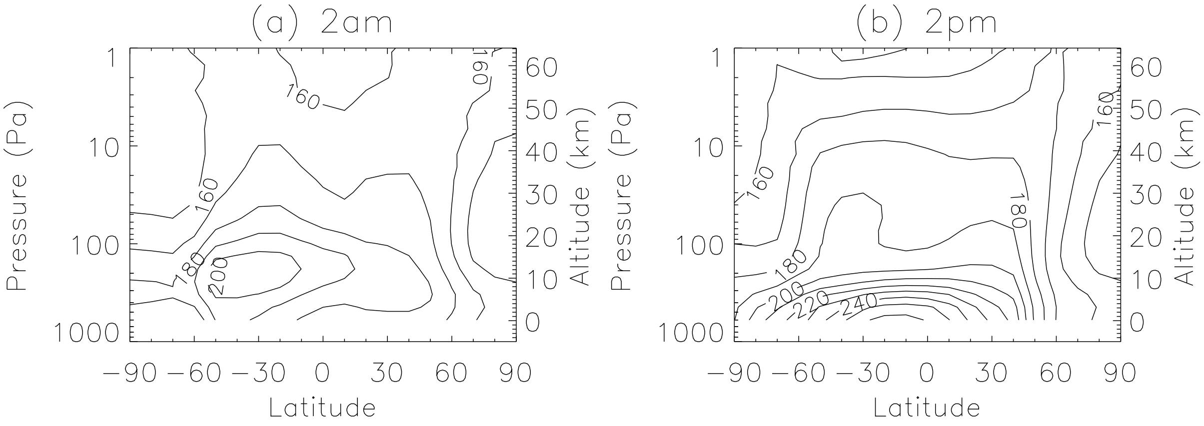

Figure 17: Temperatures at (a) 2am and (b) 2pm local time retrieved by Santee and Crisp (1993) from the IRIS instrument aboard the Mariner 9 mission. The contour interval is 10K.

erage and range from $L_s = 343°$ to $L_s = 348°$ (late northern summer) during moderately dusty conditions. Figure 17 show the 2am and 2pm temperature fields given by Santee and Crisp (1993). Note the 'hot spots' over the polar regions, i.e. regions of reversed latitudinal temperature gradient at upper levels (above approximately 30-40 km). These reversals are indicative of some dynamical process (possibly gravity wave drag) forcing the atmosphere away from radiative equilibrium, which would have both poles colder than the equator at this season.

We shall use these temperature observations to tune the gravity wave drag parameters of the sub-grid scale orographic scheme, G and Ri_c, by minimising the error, in some sense, between the observations and the model. There are no observations to constrain the low level drag component of the scheme so we merely take physically plausible values for the parameters. In fact the model climatology is not greatly sensitive to the specification of these parameters when compared to the gravity wave drag component.

Control Integration: No Gravity Wave Drag

The Oxford version of the GCM was set up at T21 resolution with 20 levels in the vertical extending to approximately 80 km. The dust distribution was set as that given by Santee and Crisp (1993), having a vertical distribution of dust absorption coefficient,

$$k(p) = k_s \exp\left(0.01\left(1 - \frac{p_s}{p}\right)\right) \tag{4}$$

where p is the pressure, p_s the surface pressure and k_s can be found by integrating

$$\tau = \int_0^{p_s} k_s \exp\left(0.01\left(1 - \frac{p_s}{p}\right)\right) dp \tag{5}$$

where $\tau$is the column-integrated dust optical depth. The horizontal distribution was set using an 8^{th} order polynomial fit to figure 9 of Santee and Crisp (1993), i.e.

$$\begin{aligned} \tau = \; & 0.88587223 - 7.9095944 \times 10^{-3} \times \phi \\ & -8.9107389 \times 10^{-6} \times \phi^2 + 2.1315059 \times 10^{-6} \times \phi^3 \\ & -9.5126781 \times 10^{-8} \times \phi^4 - 1.2816237 \times 10^{-10} \times \phi^5 \\ & +1.7927824 \times 10^{-11} \times \phi^6 - 2.0975054 \times 10^{-15} \times \phi^7 \\ & -9.4719449 \times 10^{-16} \times \phi^8 \end{aligned} \tag{6}$$

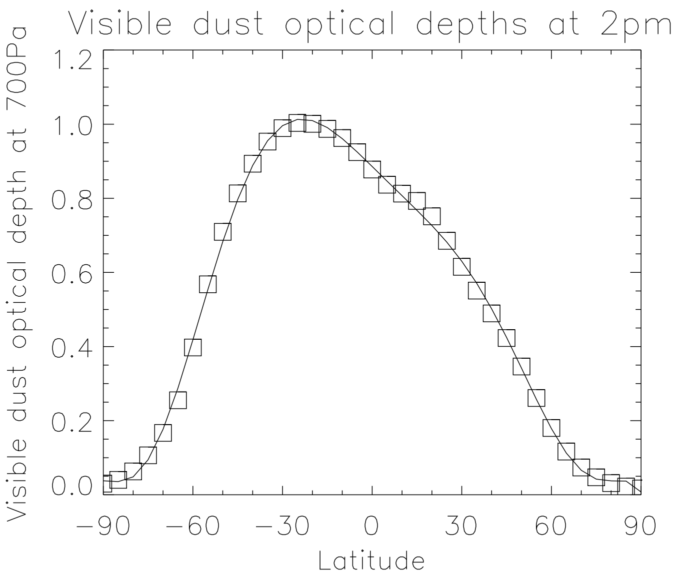

Figure 18: Visible column dust optical depth from Santee and Crisp (1993). Squares show the retrieved dust and the solid line shows an 8th order polynomial fit to those values (eq. (6)).

This is shown in figure 18.

In the first instance the model was run out to day 600 ($L_s = 323°$) with no sub-grid scale orographic scheme. The model state at day 600 was then used as the initial condition for all the subsequent sensitivity experiments. Each experiment was run out until day 647.6 ($L_s = 348°$) and the model history was sampled 5 times a day for the last 10 days of this run to correspond with the period covered by the observations ($L_s = 343°$ to $L_s = 348°$).

Figure 19 shows the 2am and 2pm temperatures from the control run (no sub-grid scale orographic scheme) as well as the difference between these fields and the observations shown in figure 17. There are large differences, greater than 30K in some regions, between the model and the observations. In particular we note that in both the southern and northern polar regions at upper levels the model is colder than the observations. This is precisely the sort of error that is probably due to the lack of gravity wave drag in the model.

Impact of the Sub-grid Scale Orographic Scheme

Now we assess the impact of the sub-grid scale orographic scheme. The model was run out from day 600 with the scheme implemented and the results sampled as before. The tunable parameters we set at $H_{NC} = 1.0, C_d = 1.0, G = 1.0$ and $Ri_c = 0.25$. Figure 20 shows the 2am and 2pm temperature fields as well as the differences from the observations for this run. In the equatorial regions and in middle latitudes the scheme has had little impact, while in the polar regions at upper levels the temperatures are now warmer than the observations. This indicates that the gravity wave drag is too strong. Figure 21 shows the impact of the gravity wave drag on the model in terms of the temperature change it can induce. The scheme can only change the temperature at upper levels in the polar regions hence we can only expect to fit the temperature in these regions. Errors in equatorial and middle latitudes must be due to other model deficiencies.

Best Fit Case

The best fit between the model and the observations was picked from over 20 sen-

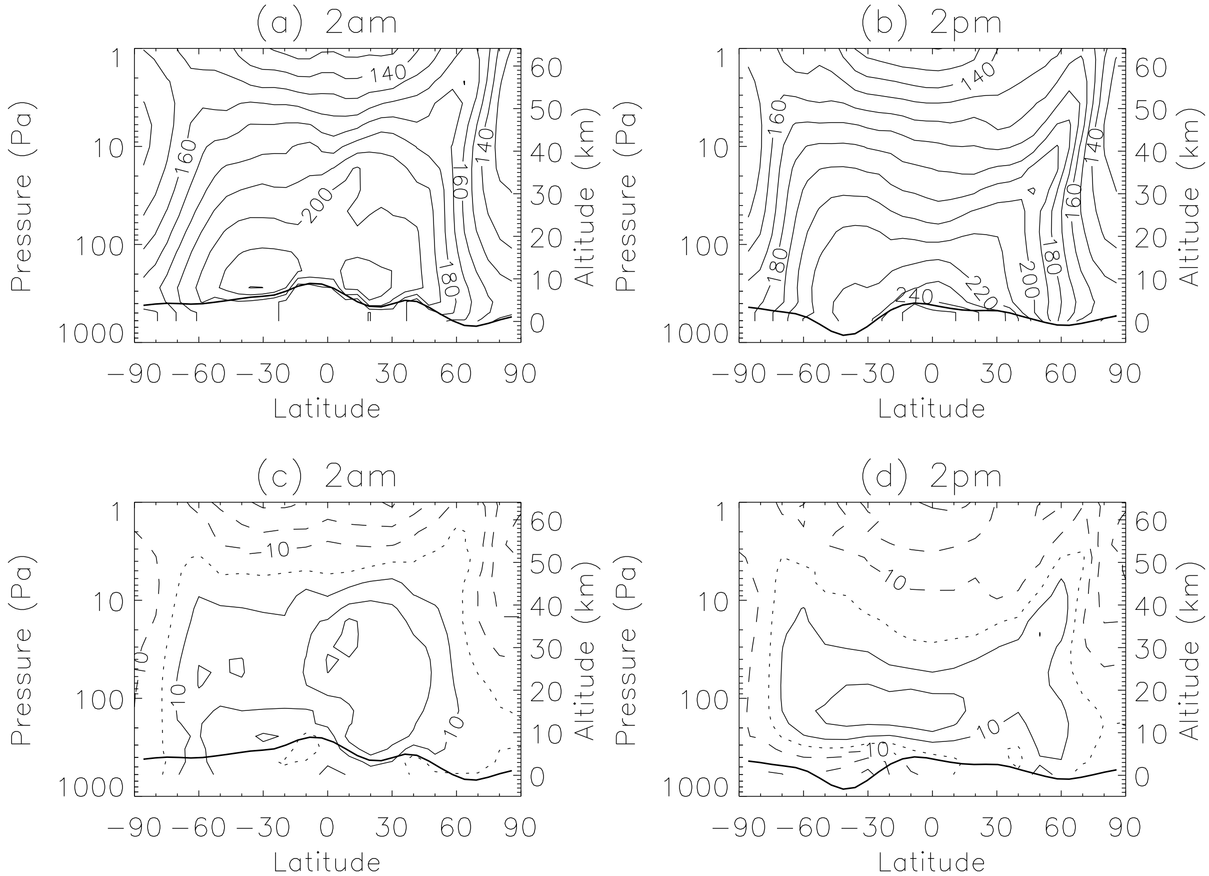

Figure 19: Model temperatures from the integration with no sub-grid scale orographic scheme. (a) 2am temperature, (b) 2pm temperature, (c) difference between the model and the observations at 2am, (d) difference between the model and the observations at 2pm. Solid contours indicate positive values, dashed contours negative and the zero contour is dotted. The contour interval is 10K in each plot. The thick black line represents the model orography.

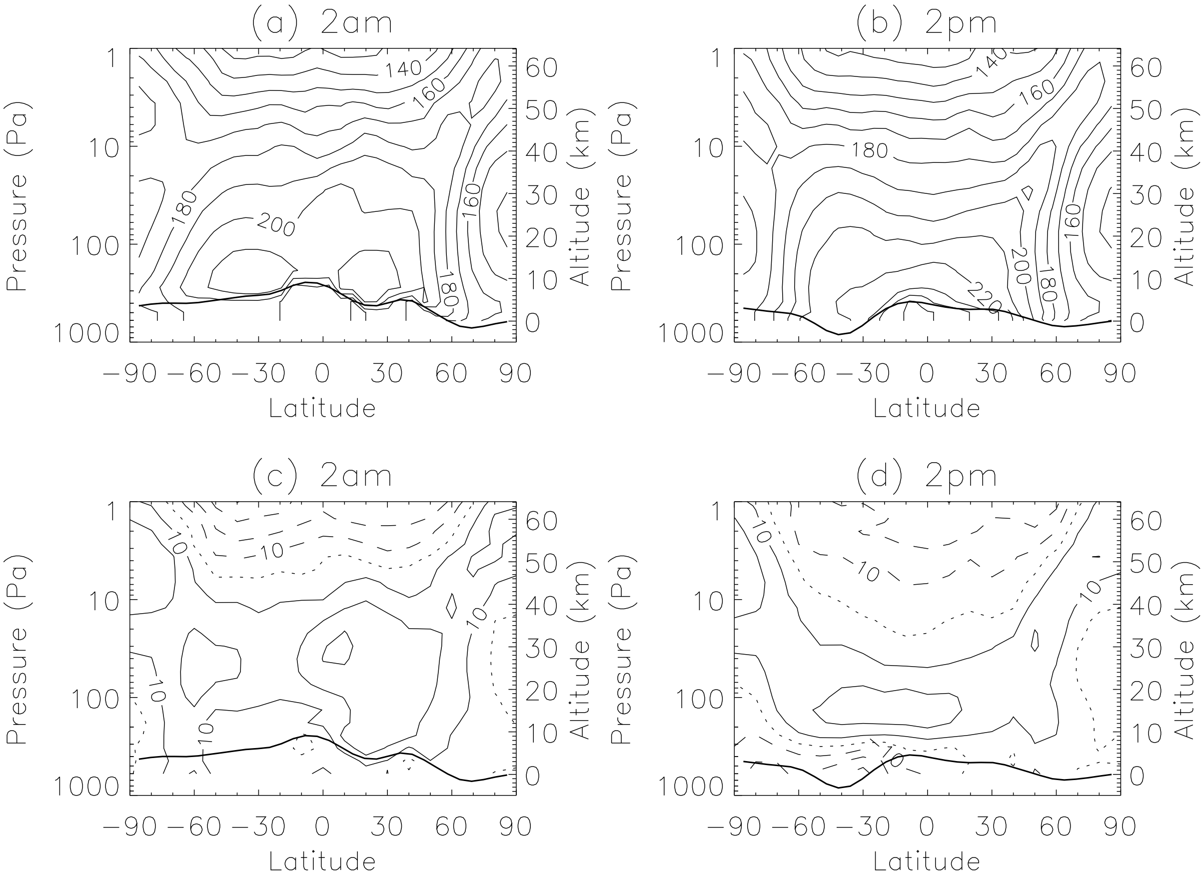

Figure 20: Model temperatures from the integration with the first guess sub-grid scale orographic scheme. (a) 2am temperature, (b) 2pm temperature, (c) difference between the model and the observations at 2am, (d) difference between the model and the observations at 2pm. Solid contours indicate positive values, dashed contours negative and the zero contour is dotted. The contour interval is 10K in each plot. The thick black line represents the model orography.

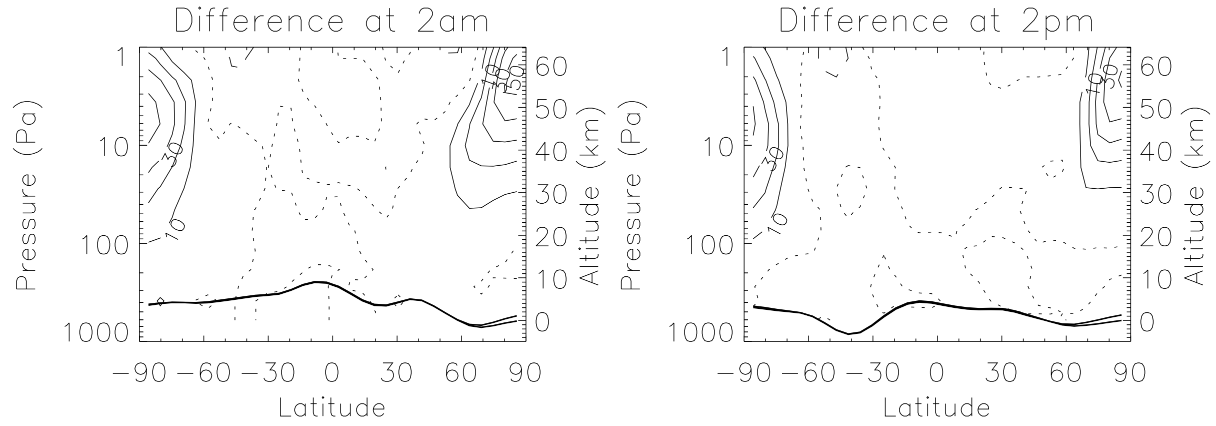

Figure 21: Temperature difference between the model run with the sub-grid scale orographic schemeand without the sub-grid scale orographic scheme. Gravity wave drag causes a warming at upper levels in the polar regions but does not affect the temperature elsewhere. Solid contours indicate positive values, dashed contours negative and the zero contour is dotted. The contour interval is 10K in each plot. The thick black line represents the model orography.

sitivity studies and is achieved with $H_{NC} = 1.0, C_d = 1.0, G = 0.1$ and $Ri_c = 0.25$. Figure 22 shows again the 2am and 2pm temperatures and error fields for this simulation. The error field is less than 10K at upper levels in the north polar regions which is within the retrieval error of the observations. The errors in the southern polar regions are somewhat higher, but it seems that this is the best fit we could obtain. These values will be assumed for the database integrations and are default in the model.

Final Validation: Best Fit Case

The best fit case for the final validation of the model i.e. the validation with the all the new physical parametrisation schemes, is shown in figure 23. The parameters for this run are $H_{NC} = 1.0, C_d = 1.0, G = 0.1$ and $Ri_c = 0.25$. The difference between the model and the observations is less than 10K in the polar regions which is well within the projected errors in the observations.

5 Polar cap scheme validation

The new polar cap scheme is composed, on the one hand, of the condensation sublimation scheme which computes the condensation and sublimation rates on the ground and in the atmosphere, and, on the other hand, of the "CO_2 snow scheme" which decreases the cap emissivity with the atmospheric condensation to simulate the impact of the observed "low emission zones".

The condensation sublimation scheme itself is based on physical laws that does not require the use of tunable parameters (to be sure that the code perform flawlessly we have conducted basic test in one and three dimensions). However, the formation and the sublimation of the polar caps is primarily controlled by the radiative balance of the polar regions (Hourdin et al., 1995) , which in turn depends on model parameters and variables such as the surface temperatures of the polar caps, the cap emissivity (and thus the low emission zones), and the cap albedo. Therefore, to validate the model, we have performed specific studies related to these quantities and tested the model ability to reproduce the general forms of the cap

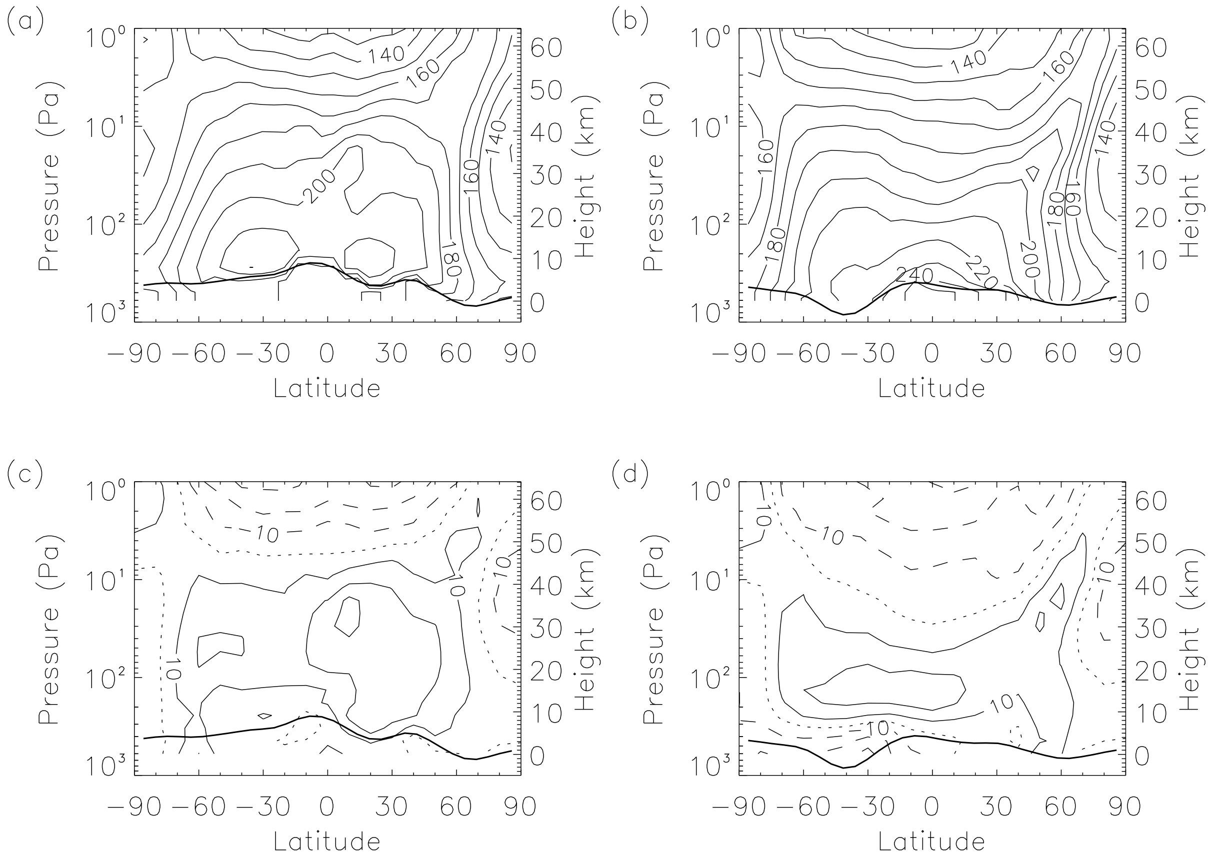

Figure 22: Model temperatures from the best fit integration with the odl GCM. (a) 2am temperature, (b) 2pm temperature, (c) difference between the model and the observations at 2am, (d) difference between the model and the observations at 2pm. Solid contours indicate positive values, dashed contours negative and the zero contour is dotted. The contour interval is 10K in each plot. The thick black line represents the model orography.

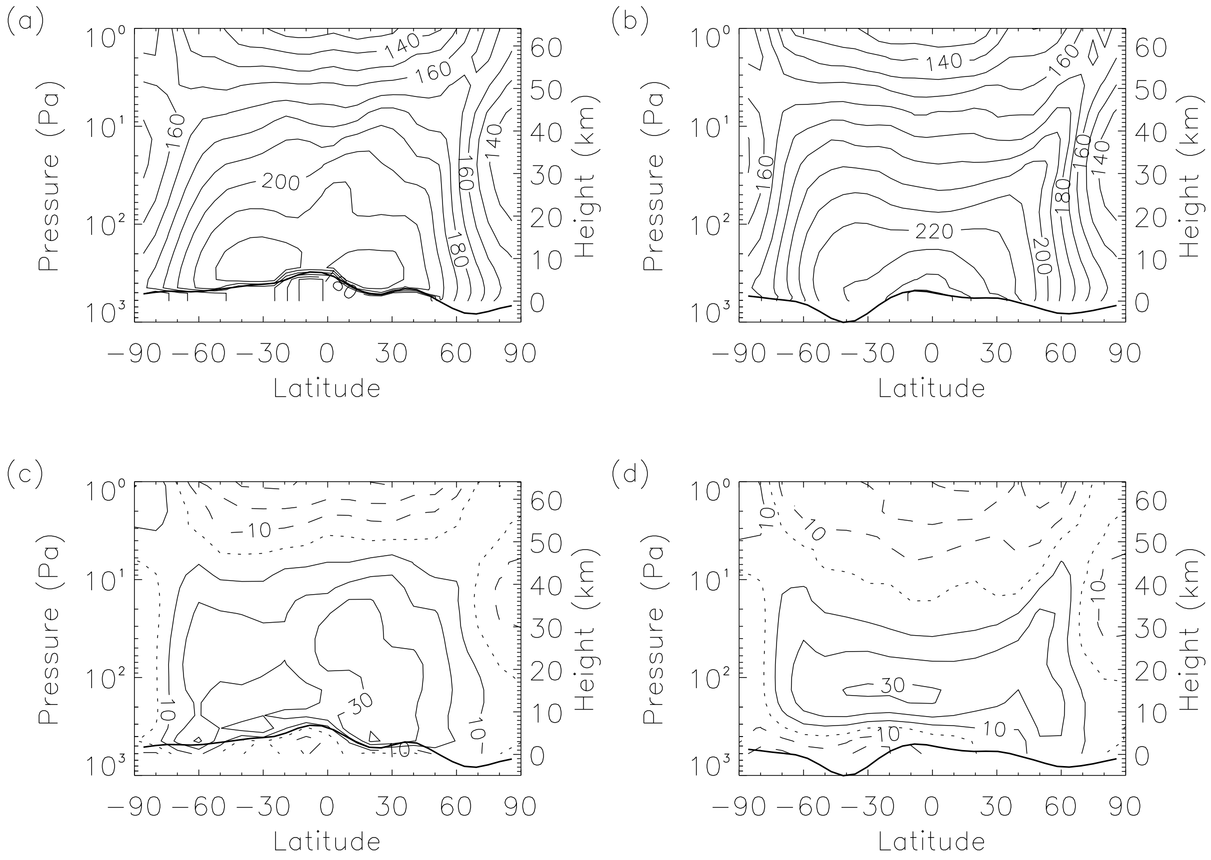

Figure 23: Model temperatures from the best fit integration using the final ESA version of the model. (a) 2am temperature, (b) 2pm temperature, (c) difference between the model and the observations at 2am, (d) difference between the model and the observations at 2pm. Solid contours indicate positive values, dashed contours negative and the zero contour is dotted. The contour interval is 10K in each plot. The thick black line represents the model orography.

seasonal evolution and in particular the annual pressure variations recorded by the Viking Landers.

5.1 Polar cap surface temperatures

The CO_2 ice surface temperature T_{surf} only depends on the local atmospheric pressure p, through the CO_2 vapor pressure curve. It is thus closely related to the local topography and the atmospheric circulation. On the basis of their analysis of the Viking IRTM data, Forget et Pollack (1995) have recently retrieved the actual surface temperatures of the polar caps (or more exactly the maximum emission temperature of the surface of the polar caps). Because the radiative budget is controlled by this quantity, it was important to check the ability of the model for simulating such temperatures. Fig. 24 shows the zonal averaged frost point temperatures computed by the GCM (resolution $64 \times 48 \times 15$) compared to the surface temperature derived from the IRTM observations. In all of the simulations, the atmospheric mass was adjusted to match the surface pressure observed at the Viking Lander 1 site at winter solstice. The most variable (and uncertain) parameter being the dust optical thickness, experiments were conducted with various mean atmospheric opacity. The polar surface temperatures were found to be not significantly sensitive to this parameter, set to 0.2 for the results shown in Fig. 24. Results obtained with both the Mars Consortium topography dataset (previously used in the LMD GCM) and the DTM topography dataset (chosen for the ESA project) are shown in Fig. 24. The modeled frost point of CO_2 appear to be warmer than the surface temperatures retrieved from the IRTM data. This is especially true with the Consortium data set in the southern hemisphere, but the DTM is also 2-3 K warmer than the observed temperature. To account for this discrepancy, we have set the maximum cap surface emissivity to 0.95, as for the rocky surface elsewhere on the planet (0.95 can thus be considered as the emissivity of the ground "below the ice") The agreement is then much better in both polar regions, as shown in Fig. 24.

5.2 Simulation of the low emission zones

To compare the low emission zones simulated in the model with the actual ones, we have modeled the brightness temperatures T_{20} measured by the IRTM instrument at 20-μm. In practice, T_{20} is computed from the modeled surface temperature and cap emissivity using results from the CO_2 cloud and snow radiative transfer models described in Forget et al. (1995).

Fig. 25 shows an example of T_{20} temperatures field simulated by the GCM during the southern winter (resolution $64 \times 48 \times 15$). For this simulation, the snow emissivity scheme parameters were set to values expected from physical considerations (100μm for the mean CO_2 snow particle radius r, and 0.5 day for the metamorphism timescale $\mathcal{T}$) with no particular tuning. Yet, the spatial scale and the intensity of the low emission zones are very close to the actual observations (See fig. 7 in Kieffer et al., 1976).

More detailed comparisons are presented in figs. 26, 27 and 28 where we show the observed and the simulated distribution of the low emission zones, identified by the difference between T_{20} and the cap surface temperatures. There again, the snow emissivity scheme parameters were not tuned. However, we used different values of the atmospheric dust optical depth τ (by its radiative effects, the dust influences the atmospheric condensation rate). We found that, with these particular snow parameters, the low emission zones distributions were very well simulated with $\tau = 0$ in the southern hemisphere (Fig. 26) , $\tau = 0.5$ in the northern hemisphere during the period preceding the global dust storm which occurred in early winter (Fig. 27), and $\tau = 1$ also in the northern hemisphere for the "colder" period following

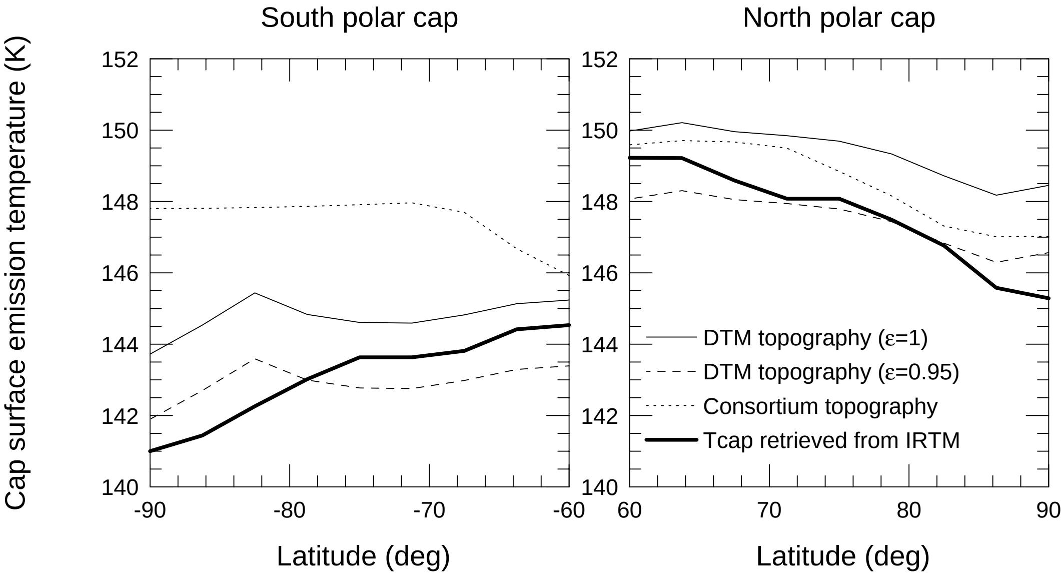

Figure 24: Comparison between zonally-averaged surface temperatures calculated by the GCM using the DTM and Consortium topography data sets with the surface temperature retrieved from the IRTM data by Forget and Pollack (1995).

the dust storm (Fig. 28). These dust optical depths are lower than the ones then observed by the Viking Landers, but their relative values are very realistic. In any case, these results show that the CO_2 snow scheme is physically sound.

5.3 Tuning the cap albedo and the CO_2 snow parameters

The Viking pressure measurements provide informations on the amount of CO_2 condensing in the polar caps, and on the global condensation and sublimation rates. Hourdin et al. (1995) performed some best fit simulations and showed that it was possible to closely match the Viking measurements using a method based on the sensitivity of the modeled atmospheric pressure to the modeled cap albedo and emissivity. Such a method calculate "best fit values" for the poorly known cap albedos as well as for the cap emissivities. The cap emissivities were then set constant in time and space in each hemisphere. In the new version of the model, the emissivity is now controlled by the CO_2 scheme parameters r and $\mathcal{T}$. In fact, we have found that, on average, the global cap emissivity is only function of the ratio $r/\mathcal{T}$. Thus the best fit procedure of Hourdin et al. (1995) can be applied on the cap albedos on the one hand, and on the ratio $r/\mathcal{T}$ on the other hand, the relative value of $\mathcal{T}$ and r being given by the observations of the low emission zones described above.

References

D. G. Andrews, J. R. Holton, and C. B. Leovy. *Middle Atmosphere Dynamics*. Academic Press, 1987.

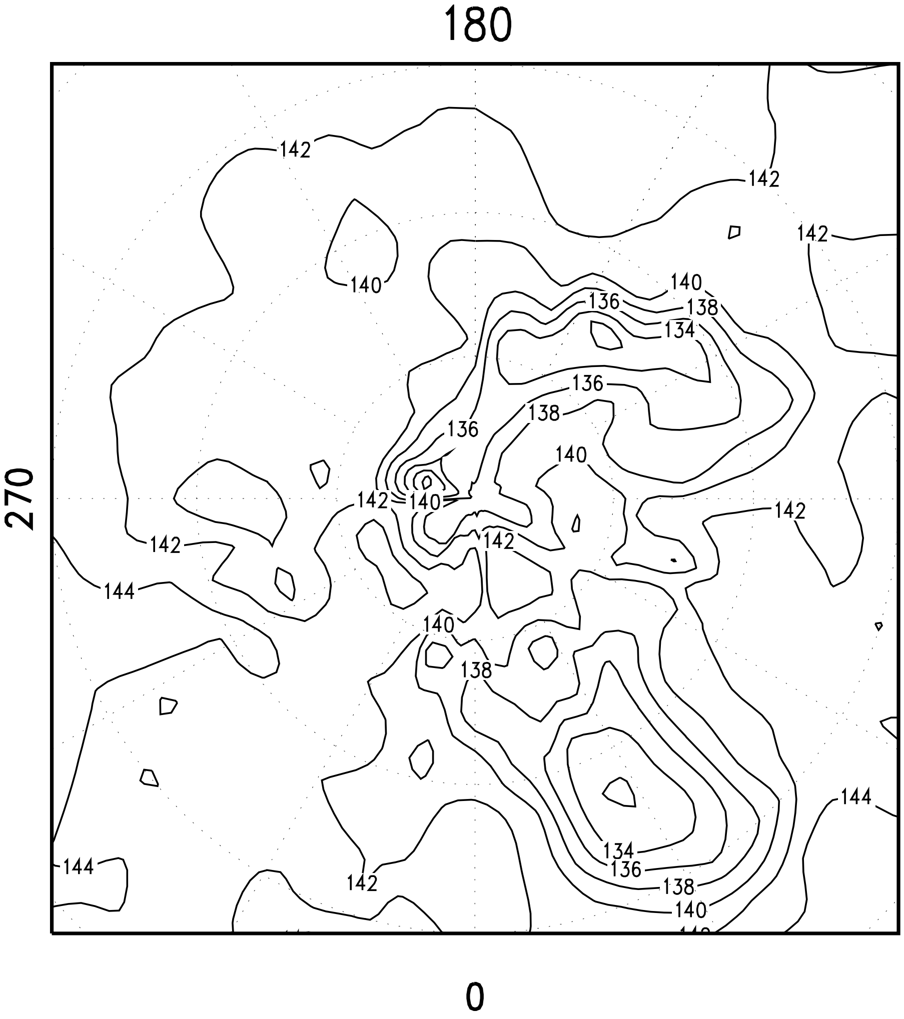

Figure 25: Simulation of IRTM T_{20} Brightness temperatures in the south polar regions

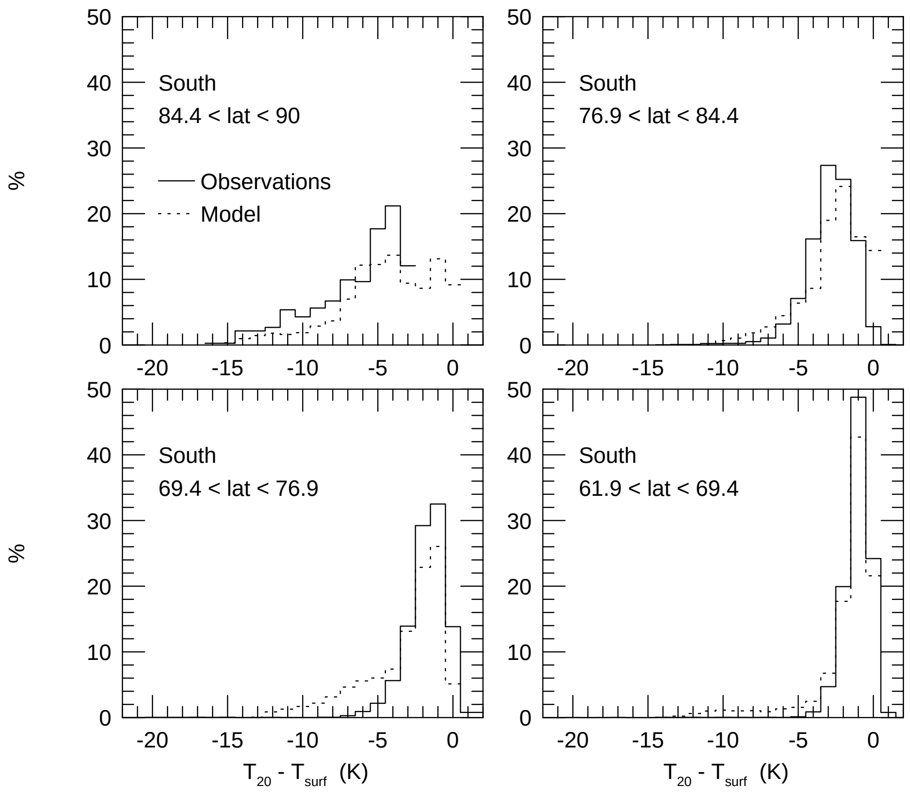

Figure 26: Comparisons of the low emission zones distribution observed by Viking in the southern hemisphere during $L_s = 90 - 120^0$ and simulated by the GCM (from a 15 days run corresponding to $L_s = 113 - 121^o$). The low emission zones are identified by the difference between the brightness temperature T_{20} and the cap surface temperature. In the model, the mean CO_2 snow particle radius r is 100μm and the snow metamorphism timescale $\mathcal{T}$ is 0.5 days The dust optical depth τ is set to 0.

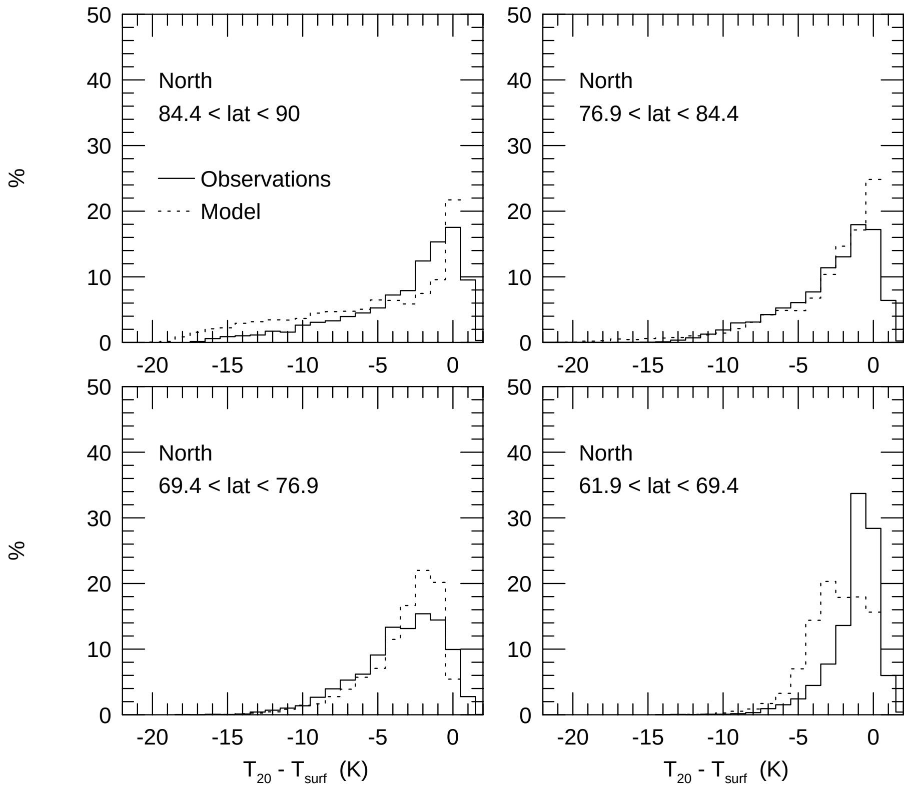

Figure 27: Same as fig. 26 in the northern hemisphere with the IRTM observations obtained before the global dust storm b ($L_s = 240 - 270^o$) and a 15 days simulations ($L_s = 260 - 270$) with $\tau = 0.3$

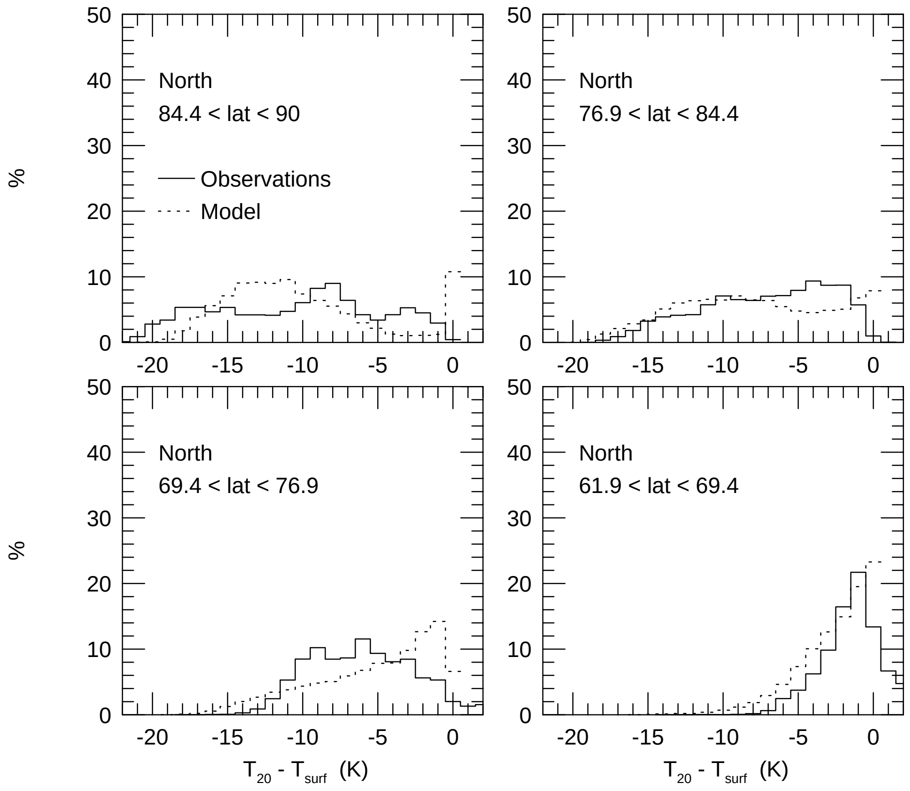

Figure 28: Same as fig. 26 in the northern hemisphere with the IRTM observations obtained after the global dust storm b ($L_s = 290 - 310^o$) and a 15 days simulations ($L_s = 260 - 270$) with $\tau = 1$

F. Forget, J. B. Pollack, and G. B. Hansen. Low brightness temperatures of Martian polar caps : CO_2 clouds or low surface emissivity? *J. Geophys. Res.*, 100:21,119–21,234, 1995.

H. M. Helfand and J. C. Labraga. Design of a nonsingular level 2.5 second-order closure for the prediction of atmospheric turbulence. *J. Atmos. Sci.*, 45:113–132, 1988.

F. Hourdin, F. Forget, and O. Talagrand. The sensitivity of the Martian surface pressure to various parameters: A comparison between numerical simulations and Viking observations. *J. Geophys. Res.*, 100:5501–5523, 1995.

Hugh H. Kieffer, S. C. Chase, E. D. Miner, Frank Don. Palluconi, Guidoa Münch, Gerry Neugebauer, and Terry Z. Martin. Infrared thermal mapping of the Martian surface and atmosphere: First results. *Science*, 193:780–786, 1976.

George L. Mellor and Tetsuji Yamada. A hierarchy of turbulence closure models for planetary boundary layers. *J. Atmos. Sci.*, 31:1791–1806, 1974.

George L. Mellor and Tetsuji Yamada. Development of a turbulence closure model for geophysical fluid problems. *Review of Geophys. and Space Phys.*, 20(4):851–875, 1982.

T. N. Palmer, G. J. Shutts, and R. Swinbank. Alleviation of a systematic westerly bias in general circulation and numerical weather prediction models through an orographic gravity wave drag parametrisation. *Q. J. R. Meteorol. Soc.*, 112: 1001–1039, 1986.

Michelle Santee and David Crisp. Thermal structure and dust loading of the Martian atmosphere during late southern summer: Mariner 9 revisited. *J. Geophys. Res.*, 98:3261–3279, 1993.

O. B. Toon, C. P. McKay, T. P. Ackerman, and K. Santhanam. Rapid calculation of radiative heating rates and photodissociation rates in inhomogeneous multiple scattering atmospheres. *J. Geophys. Res.*, 94:16,287–16,301, 1989.